



Chemical Compositions of Field and Globular Cluster RR Lyrae Stars. I. NGC 3201*

D. Magurno^{1,2}, C. Sneden³, V. F. Braga^{4,5}, G. Bono^{1,2}, M. Mateo⁶, S. E. Persson⁷, M. Dall’Ora⁸, M. Marengo⁹,
M. Monelli¹⁰, and J. R. Neeley¹¹

¹ University of Roma Tor Vergata, via della Ricerca Scientifica 1, I-00133, Roma, Italy; davide.magurno@roma2.infn.it

² INAF Osservatorio Astronomico di Roma, via Frascati 33, I-00040, Monte Porzio Catone RM, Italy

³ Department of Astronomy and McDonald Observatory, The University of Texas, Austin, TX 78712, USA

⁴ Instituto Milenio de Astrofísica, Santiago, Chile

⁵ Departamento de Física, Facultad de Ciencias Exactas, Universidad Andrés Bello, Fernández Concha 700, Las Condes, Santiago, Chile

⁶ Department of Astronomy, University of Michigan, 1085 S. University, Ann Arbor, MI 48109, USA

⁷ Observatories of the Carnegie Institution for Science, 813 Santa Barbara Street, Pasadena, CA 91101, USA

⁸ INAF Osservatorio Astronomico di Capodimonte, Salita Moiariello 16, I-80131 Napoli, Italy

⁹ Department of Physics and Astronomy, Iowa State University, A313E Zaffarano, Ames, IA 50010, USA

¹⁰ IAC—Instituto de Astrofísica de Canarias, Calle Via Lactea, E38200 La Laguna, Tenerife, Espana

¹¹ Department of Physics, Florida Atlantic University, Boca Raton, FL 33431, USA

Received 2018 June 25; revised 2018 July 16; accepted 2018 July 17; published 2018 August 30

Abstract

We present a detailed spectroscopic analysis of horizontal branch stars in the globular cluster NGC 3201. We collected optical (4580–5330 Å), high-resolution ($\sim 34,000$), high signal-to-noise ratio (~ 200) spectra for 11 RR Lyrae stars and one red horizontal branch star with the multifiber spectrograph M2FS with the 6.5 m Magellan telescope at the Las Campanas Observatory. From measured equivalent widths, we derived atmospheric parameters and abundance ratios for α (Mg, Ca, and Ti), iron-peak (Sc, Cr, Ni, and Zn), and s -process (Y) elements. We found that NGC 3201 is a homogeneous, monometallic ($[\text{Fe}/\text{H}] = -1.47 \pm 0.04$), α -enhanced ($[\alpha/\text{Fe}] = 0.37 \pm 0.04$) cluster. The relative abundances of the iron-peak and s -process elements were found to be consistent with solar values. In comparison with other large stellar samples, NGC 3201 RR Lyraes have similar chemical enrichment histories as do those of other old ($t \geq 10$ Gyr) Halo components (globular clusters; red giants; blue and red horizontal branch stars; and RR Lyraes). We also provided a new average radial velocity estimate for NGC 3201 by using a template velocity curve to overcome the limit of single-epoch measurements of variable stars: $V_{\text{rad}} = 494 \pm 2 \text{ km s}^{-1}$ ($\sigma = 8 \text{ km s}^{-1}$).

Key words: globular clusters: individual (NGC 3201) – stars: abundances – stars: variables: RR Lyrae – techniques: spectroscopic

Supporting material: machine-readable tables

1. Introduction

Dating back to Baade (1958), RR Lyrae stars (RRL) have played a fundamental role as tracers of old ($t > 10$ Gyr) stellar populations. RRLs are ubiquitous, having been identified both in gas-poor and in gas-rich stellar systems. Moreover, they can be easily identified, thanks to a particular coupling between pulsation period and shape/amplitude of their optical light curves. Therefore, they have been extensively used to investigate the early formation and the spatial structure of the Galactic bulge (Pietrukowicz et al. 2015) and of the Galactic halo (Drake et al. 2013; Torrealba et al. 2015). The RRLs in globulars have been widely used not only to constrain the evolutionary properties of old, low-mass, central helium-burning stars, but also to investigate the impact that the intrinsic parameters (metallicity) and the environment have on the topology of the instability strip and on their pulsation properties (Oosterhoff 1939; van Albada & Baker 1973; Caputo 1997; Bono et al. 2007).

RRLs are also very good distance indicators. Dating back once again to Baade & Swope (1955) and to Sandage (1958), it was shown that RRLs have a well-defined visual magnitude–metallicity relation. Their use as standard candles became even more compelling, thanks to the empirical discovery by Longmore

et al. (1986, 1990) that RRLs have near-infrared, period–luminosity correlations. More recent empirical and theoretical evidence indicate that in the near-infrared (NIR) they obey period–luminosity–metallicity (PLZ) relations (Bono et al. 2003; Braga et al. 2015, 2018; Marconi et al. 2015; Neeley et al. 2017).

The RRLs have also played a crucial role in the investigation of the spatial distribution of old stellar populations in nearby dwarf galaxies (Magellanic Clouds: Soszyński et al. 2009; Carina: Coppola et al. 2013; Sculptor: Martínez-Vázquez et al. 2016b). The *Hubble Space Telescope* (HST) optical photometry played a fundamental role in detecting and tracing RRLs in satellites of M31 (Clementini et al. 2001; Pritzl et al. 2002; Monelli et al. 2017), and in galaxies of the Sculptor group (da Costa et al. 2010). The pulsation properties of RRLs in globulars, and in Local Group ($d < 1$ Mpc) and Local Volume ($d < 10$ Mpc) galaxies, can be adopted to constrain the early formation and evolution of the Galactic spheroid (Stetson et al. 2014; Fiorentino et al. 2015).

RRLs in globular clusters are especially useful for several reasons. First, the ages and the chemical compositions of many clusters are well known. In particular, the iron metallicities, α and neutron-capture elements have been studied extensively, (e.g., Carretta et al. 2009a). Second, the evolutionary status and the topology of the instability strip is also well established (Walker et al. 2017). The globulars hosting a sizable sample of RRLs allow us to investigate the regions of the instability strip in which variables pulsate either as first overtones (hotter) or as

* This paper includes data gathered with the 6.5 m Magellan Telescopes located at Las Campanas Observatory, Chile.

fundamentals (cooler). Moreover, we can also estimate the width in temperature of the region in which RRLs pulsate simultaneously in the first overtone and in the fundamental mode, i.e., the so-called mixed mode pulsators. Finally, evolved cluster RRLs can be more easily identified, as they attain luminosities that are systematically brighter than the zero-age horizontal branch (ZAHB) luminosity level.

Metallicities and detailed abundance ratios of individual stars are crucial not only to provide more accurate individual distance determinations, but also to trace the early chemical enrichment of old stellar populations (Monelli et al. 2012; Martínez-Vázquez et al. 2016a). Metallicities of field RRLs have been derived from the large and homogeneous SDSS DR8 sample of medium resolution spectra (Lee et al. 2011; Drake et al. 2013), using several different techniques, mostly based on photometric indices (Mateu et al. 2012) or on metallicity indicators like the Ca II K lines (ΔS , Preston 1959; Layden 1994). Recently, metallicities for field RRLs have been estimated using several spectroscopic indicators and collected at different pulsation phases.

High-resolution spectroscopic analyses of field RRLs are currently limited to ~ 140 stars (e.g., Clementini et al. 1995; Liu et al. 2013; Pancino et al. 2015; Chadid et al. 2017; Sneden et al. 2017; Andrievsky et al. 2018). These studies have lagged compared with those of other groups of variables stars (Classical Cepheids, Miras) for many reasons.

- (a) Pulsation periods of RRLs range from a few hours for first overtone, RRc, pulsators to almost one day for fundamental, RRab, pulsators. This means that the exposure time to collect spectra can hardly be longer than 30–45 minutes to avoid velocity smearing of spectra. To acquire high-resolution and signal-to-noise (S/N) spectra typically requires using 4–8 m class telescopes, or co-adding spectra obtained over many pulsation cycles by smaller telescopes. This requires well-known pulsational timing to avoid overlap of different phases, and in turn different physical properties.
- (b) RRab stars experience several nonlinear phenomena during their pulsation cycles. The formation and propagation of strong shocks across the rising-light branch cause line doubling and P Cygni profiles (Preston 1959; Preston & Paczynski 1964). During these pulsation phases, the assumption of quasi-static atmospheres is no longer valid, as the line formation takes place in a medium affected by sharp temperature and density gradients (Bono et al. 1994).
- (c) Up to 50% of RRab stars exhibit a Blazhko effect (Kolenberg et al. 2010b; Benkő et al. 2014), i.e., a quasi-periodic (tens to hundreds of days) modulation of the light-curve amplitude and period (Jurcsik et al. 2009; Kolenberg et al. 2010a). Many hypothesis have been formulated to explain the Blazhko effect. Recently, Buchler & Kolláth (2011) suggested that the modulation is the consequence of resonance between the fundamental and the ninth overtone pulsation modes; however, we still lack agreement on a convincing physical explanation.
- (d) The RRLs cover a very broad metallicity range. Current estimates suggest a range from $[\text{Fe}/\text{H}] \simeq -2.9$ (Govea et al. 2014) to $[\text{Fe}/\text{H}] \simeq 0.1$ (Chadid et al. 2017).¹² The identification and measurement of individual atomic lines

requires high spectral resolution. Such lines are not plentiful in RRLs, which have temperatures $T_{\text{eff}} \simeq 6000\text{--}8000$ K and surface gravities $\log g \simeq 2.5 \pm 0.5$ (Bono & Stellingwerf 1994; Marconi et al. 2015).

In this paper, we report an abundance analysis on eleven RRLs and one red horizontal branch (RHB) star in the globular cluster NGC 3201, using high-resolution optical spectra collected with M2FS at Magellan. We have derived $[\text{Fe}/\text{H}]$ metallicities and abundance ratios $[\text{X}/\text{Fe}]$ of α -elements (Mg, Ca, and Ti), iron-peak elements (Sc, Cr, Ni, and Zn) and one s -process element (Y). This GC has been widely investigated using giant branch (RGB, AGB) stars (e.g., Carretta et al. 2009a), and it is generally accepted to be a monometallic cluster ($[\text{Fe}/\text{H}] \sim -1.5$), but an extended analysis of its RRLs has not been previously done. The only RRL-based analysis of NGC 3201 was performed by Smith & Manduca (1983), who estimated iron abundances using the ΔS technique. Therefore, our main goal is to obtain a new independent abundance analysis for NGC 3201 based on RRLs and to compare it with results available in the literature for RGB and AGB stars. In Section 2 we describe the instrument and the data sample. In Section 3, we discuss the radial velocity analysis. Section 4 focuses on abundance determinations and comparison with other globular clusters and field stars. Finally, Section 5 summarizes the current results.

2. Instrument and Data Sample

In 2015 February, we collected spectra for 11 RRLs and one RHB star in the globular cluster NGC 3201 (Figure 1) using the Michigan/Magellan Fiber System (M2FS; Mateo et al. 2012) installed at the Magellan/Clay 6.5 m telescope at the Las Campanas Observatory in Chile. The spectrograph configuration used an order-isolation filter to limit the spectral coverage to 4580–5330 Å in 11 overlapping echelle orders. A total of eight stars could be observed with one setup with each of the two camera/detector units, or 16 stars in all. The spectrograph entrance slit size was 95 μm , which yielded spectra with resolving power $R \equiv \lambda/\Delta\lambda \simeq 34,000$.

All the observed variables are RRab, including V38 which is also a Blazhko candidate (Layden & Sarajedini 2003; J. R. Neeley et al. 2018, in preparation). It is possible to deduce the nature of V38 from its characteristic light curve (Figure 2). Unfortunately, only for two stars (V41 and V47) is very recent photometry available by ASAS-SN (Shappee et al. 2014; Jayasinghe et al. 2018). The other variables have photometry from one to more than 10 years older than our spectra, so that the phase determination could be affected by some inaccuracy. Average magnitudes and new estimated periods are listed in Table 1.

3. Radial Velocities

The radial velocities of the sample were estimated using the task *fxcor* in IRAF (Tody 1986, 1993),¹³ by cross-correlation of the overall spectral range with a synthetic spectrum. The synthetic spectrum was generated with the MOOG driver *synth* (Sneden 1973), with an “average RRL” parameters setting ($T_{\text{eff}} = 6500$ K, $\log g = 2.5$, $\xi_{\text{turb}} = 3.0$ km s⁻¹), and a

¹² We adopted the standard notation, $[\text{X}/\text{H}] = A(\text{X}) - A_{\odot}(\text{X})$, where $A(\text{X}) = \log(N_{\text{X}}) - 12$. Solar abundances refer to Asplund et al. (2009) within the text.

¹³ IRAF is distributed by the National Optical Astronomy Observatories, which are operated by the Association of Universities for Research in Astronomy, Inc., under cooperative agreement with the National Science Foundation.

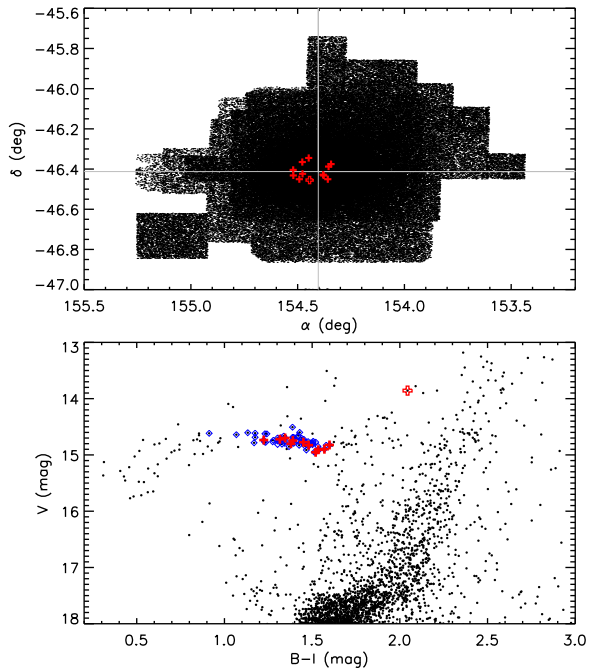


Figure 1. Top panel: radial distribution of the 12 spectroscopic stars for which we collected high-resolution optical spectra (RRLs: filled red crosses; RHB: empty red cross) in the globular cluster NGC 3201 (black dots; photometry from J. R. Neeley et al. 2018, in preparation). Bottom panel: $V, B-I$ CMD of NGC 3201. Known cluster RRLs are shown with blue diamonds.

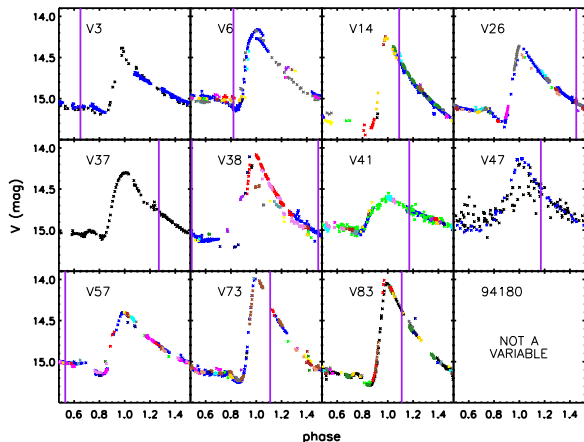


Figure 2. V-band light curves for the 11 sample RRLs. Color coding highlights different data sets. Purple vertical lines show the observed phases for the individual spectra.

metallicity comparable with the literature estimates for NGC 3201 ($[Fe/H] = -1.5$). This computed spectrum was then smoothed to the M2FS resolution ($R = 34,000$). An accurate NGC 3201 cluster radial velocity has been recently determined by Ferraro et al. (2018): $494.5 \pm 0.4 \text{ km s}^{-1}$, using 454 non-variable stars. This very large value makes it a good indicator of cluster membership for individual stars. However, we are dealing with variable stars, so the instantaneous velocities (V_{rad} , Table 2) are not good representatives of the average cluster velocity. The mean velocity obtained from our single-epoch measurements is $489 \pm 6 \text{ km s}^{-1}$. To correct for the pulsational velocities, we reconstructed the velocity curve for each star over the entire pulsation cycle by using a template (Sesar 2012). The first step was to select the template radial velocity among those available, which are based on hydrogen

(H_{α} , H_{β} , H_{γ}) or metallic lines. We chose the latter of these, as our radial velocities are based on metallic lines. After that, we used Equation (5) in Sesar (2012) to rescale the template to the appropriate amplitude of each star (Table 1, Figure 2). Using the epoch of maximum light displayed in Table 2, we have anchored the template radial velocity to the measured point and derived the systemic velocity as the integral average velocity along the pulsation cycle (V_{γ} , Table 2). Finally, we estimated the cluster radial velocity as $494 \pm 2 \text{ km s}^{-1}$, independent of phase, with a standard deviation of 8 km s^{-1} . However, assumptions about the reconstruction of the velocity curves and errors in the estimate of the epoch of maximum light affect the template results. Figure 3 shows the instantaneous radial velocities for the 12 stars in our sample and an ensemble of the template velocity curves for the 11 RRLs (shaded area). The solid and dashed purple lines show the cluster average velocity with the errors on the mean. It is clear that a correct phasing of the observation is fundamental to obtain more precise results.

4. Abundance Analysis

Metallicities and relative abundances were derived from equivalent widths (EW) of selected atomic transitions in our spectra. We prepared the atomic line list selecting only the isolated, unblended lines. We then measured their EW by mean of a multi-Gaussian fitting performed with pyEW by M. Adamow¹⁴ and visually inspected them. We discarded all the highly asymmetric lines and the ones too weak ($EW \leq 10 \text{ m\AA}$) or too strong ($EW \geq 180 \text{ m\AA}$). Weak lines could be confused within the noise, and their measurement errors are too large, whereas strong lines are on the damping portion of the curve of growth and we expected larger errors associated with the retrieved abundances. We ended up with the line list in Table 3.

We used the LTE line analysis code MOOG (Snedden 1973), implemented in the Python wrapper pyMOOGi¹⁵ (Adamow 2017), and a grid of α -enhanced models from Castelli & Kurucz (2003)¹⁶ to estimate the atmospheric parameters (T_{eff} , $\log g$, ξ_{turb}) and the abundances for the sample spectra. The entire analysis mainly concentrated on Fe I and Fe II lines to estimate the proper parameters; the final set for each star is given in Table 2. We searched for the spectroscopically defined parameters set following a standard approach. An example is shown in Figure 4.

- (i) The effective temperature is estimated in such a way that abundances from individual lines do not show dependence on the excitation potential (EP; top panel).
- (ii) The microturbulence is estimated limiting the dependence of the individual line abundances on the reduced equivalent width ($\log(EW \lambda^{-1})$; bottom panel).
- (iii) The surface gravity is estimated assuming the balance between the ionization states, minimizing the differences between neutral and ionized species.

The EW analysis is bolstered by two other exercises with our spectra. In Figure 5, we show a montage of the spectra in the wavelength region 4830–4930 Å, ordering the stars by their derived temperatures. The dependence on T_{eff} appears: the warmer stars have weaker atomic line absorptions and stronger 4861 Å H_{β} lines. In Figure 6 we show the FWHM values for

¹⁴ <https://github.com/madamow/pyEW>

¹⁵ <https://github.com/madamow/pymoogi>

¹⁶ <http://kurucz.harvard.edu/grids.html>

Table 1
Photometric Parameters for the Sample Stars in NGC 3201

ID	α	δ	p (days)	HJD ^a	HJD ₀ ^a	phase	type	$\langle V \rangle$	Vamp	References
V3	10:17:54.47	-46:25:25.4	0.59939921	7079.77870	4123.15325	0.65	RRab	14.90	0.67	N,L03
V6	10:17:26.09	-46:27:02.3	0.52561240	7079.77870	6040.73538	0.82	RRab	14.74	0.93	N,L03
V14	10:17:22.42	-46:22:31.5	0.50929203	7079.77870	6718.64605	0.09	RRab	14.95	1.12	N
V26	10:17:58.09	-46:27:01.8	0.56896113	7079.75386	6718.77606	0.45	RRab	14.90	0.92	N
V37	10:17:30.69	-46:25:55.7	0.57699328	7079.75386	4123.08217	0.27	RRab	14.78	0.78	N
V38	10:17:31.42	-46:25:41.1	0.50909990	7079.77870	6718.57488	0.49	RRab ^b	14.76	1.04	N
V41	10:18:05.02	-46:24:14.8	0.66532664	7079.75386	7961.19997	0.17	RRab	14.73	0.40	ASN,N
V47	10:17:47.56	-46:20:41.7	0.52086843	7079.75386	7960.97248	0.17	RRab	14.60	0.89	ASN,L03
V57	10:18:04.87	-46:25:54.6	0.59343497	7079.77870	6718.65687	0.53	RRab	14.83	0.74	N
V73	10:17:25.20	-46:23:15.2	0.51995506	7079.75386	6718.84703	0.11	RRab	14.75	1.22	N
V83	10:17:54.76	-46:21:54.4	0.54520516	7079.77870	6718.79059	0.11	RRab	14.79	1.23	N
94180	10:17:46.54	-46:27:17.3	...	7079.75386	RHB	13.86	...	N

Notes.^a 2450000+.^b Blazhko.**References.** N: J. R. Neeley et al. (2018, in preparation), L03: Layden & Sarajedini (2003), ASN—ASAS-SN (Shappee et al. 2014; Jayasinghe et al. 2018).

all the measured atomic lines of each star, highlighting with blue color the five RR Lyraes with highest derived T_{eff} values. The mean FWHM values range from 0.33 to 0.43 Å, larger than that which would be generated by a combination of spectrograph, thermal, and microturbulent broadening. We attribute this extra width to a combination of macroturbulent and possible rotational broadening. Upper limits to axial rotation of RRab field stars is estimated to be $\sim 5 \text{ km s}^{-1}$ (Preston et al. 2018). These stars, in comparison with the six cooler RR Lyraes, have three common characteristics: far fewer measurable lines ($\langle n_{\text{warm}} \rangle \simeq 13$ and $\langle n_{\text{cool}} \rangle \simeq 46$); larger FWHM values ($\langle \text{FWHM}_{\text{warm}} \rangle \simeq 0.40$ and $\langle \text{FWHM}_{\text{cool}} \rangle \simeq 0.35$); and phases closer to maximum light ($\langle \phi_{\text{warm}} \rangle \simeq 0.08$, $\langle \phi_{\text{cool}} \rangle \simeq 0.41$);

Some variation on the EW procedure was applied for V14. Only one Fe I line is observed in its spectrum, so that it is impossible to estimate the effective temperature as described above. However, a visual inspection of its spectrum clearly shows that the few observable lines are weaker than the counterparts in the other stars, suggesting that this star is the hottest one in the sample. Based on this visual evidence, we estimated $T_{\text{eff}} \sim 7500 \text{ K}$ for V14.

We also call attention to star 94180,¹⁷ the NGC 3201 RHB star observed along with the RR Lyrae sample. Our Fe EW analysis clearly indicated a temperature ($T_{\text{eff}} = 5600 \text{ K}$) much cooler than the red edge of the RR Lyrae instability strip. Inspection of Figure 5 confirms the EW analysis. This star has the deepest atomic lines, and its H β line has weak-to-absent damping wings. The FWHM data for 94180 (Figure 6) are in accord: this star has the largest number of measured lines (81) and the smallest measured line widths ($\langle \text{FWHM} \rangle \simeq 0.32$) of all of our stars.

Finally, in Figure 7 we compare estimated effective temperatures and surface gravities of our sample with those from some of the literature spectroscopic studies of field RR Lyrae stars. Our RRLs appear to have systematically higher gravities than the field RRLs, suggesting the latter to be slightly more evolved than the cluster stars. Moreover, the difference between the RRLs and the RHB star is evident.

¹⁷ The star is identified as 94180 in our catalog of NGC 3201 stars, provided by P. B. Stetson (2018, private communication). SIMBAD online catalog identifies it as NGC 3201 CWF3 3-327. See Table 1 for more details.

We estimated the internal errors in iron abundances associated with changes in the model parameters by varying effective temperature, surface gravity and microturbulence in the line analysis of V41, selected as a representative of the entire cluster. Variations in steps of $\Delta T_{\text{eff}} = 100 \text{ K}$, $\Delta \log g = 0.3$, $\Delta \xi_{\text{turb}} = 0.5 \text{ km s}^{-1}$ were applied, considering them as independent parameters. Results are shown in Table 4. Effective temperature and surface gravity are the main sources of error for Fe I and Fe II abundances, respectively, whereas the impact of microturbulence is on average a factor of two smaller. The total error associated with the parameters (last column in Table 4) is then computed by adding in quadrature the individual errors on the intrinsic parameters. The final estimated Fe I and Fe II abundance uncertainties due to model atmosphere uncertainties are about 0.01 dex for each species.

A comprehensive abundance analysis cannot leave possible NLTE corrections out of consideration. Several works are available in recent literature dealing with NLTE in RRL stars (Wallerstein & Huang 2010; Hansen et al. 2011; Andrievsky et al. 2018), but the analysis is far to be complete. Indeed, not all the elements we are dealing with have already been studied. NLTE corrections can affect the abundances up to ~ 0.5 dex (Hansen et al. 2011) but they are strongly dependent on temperature and the details of the calculations. Additionally, the M2FS wavelength coverage limits the number of useful transitions available to make a serious study of NLTE effects. For these reasons, we decided to take into account only LTE effects, obtaining reasonable metallicities and abundance ratios compared with RGB stars (see the next sections).

4.1. Iron Metallicity

We estimated the average iron abundance of NGC 3201 to be $\langle [\text{Fe}/\text{H}] \rangle = -1.47 \pm 0.04$, with a dispersion $\sigma = 0.14$ dex. Table 5 lists the individual iron abundances for the current sample with the intrinsic errors quantifying the line to line variability. Data listed in this table indicate that our mean $[\text{Fe}/\text{H}]$ estimate is compatible with a homogeneous, mono-metallic cluster. Note that we are dealing with variable stars and once uncertainties in the intrinsic parameters are taken into account, the monometallicity of the cluster is further supported.

NGC 3201 has been at the cross-road of several spectroscopic investigations in the recent literature (see Table 6 for a

Table 2
Instantaneous Radial Velocity, Systemic Velocity from Template, and Estimated Stellar Parameters

ID	V_{rad} (km s^{-1})	V_{γ} (km s^{-1})	T_{eff} (K)	$\log g$ (cgs)	ξ_{turb} (km s^{-1})	[M/H] (dex)
V3	497.2 ± 0.4	482 ± 8	6400 ± 100	2.5 ± 0.2	3.6 ± 0.2	-1.4 ± 0.1
V6	520.5 ± 0.8	497 ± 8	6800 ± 300	3.3 ± 0.4	2.8 ± 0.4	-1.2 ± 0.1
V14	463.5 ± 1.2	493 ± 8	7500 ± 300	3.1 ± 0.4	3.0 ± 0.4	-1.5 ± 0.1
V26	504.1 ± 0.3	497 ± 8	6000 ± 100	2.1 ± 0.1	3.5 ± 0.1	-1.8 ± 0.1
V37	468.4 ± 0.7	477 ± 8	7200 ± 300	2.5 ± 0.2	2.6 ± 0.4	-1.5 ± 0.1
V38	504.6 ± 0.4	494 ± 8	6400 ± 200	2.8 ± 0.2	2.8 ± 0.3	-1.5 ± 0.1
V41	490.1 ± 0.3	505 ± 8	6350 ± 100	2.3 ± 0.1	3.0 ± 0.1	-1.5 ± 0.1
V47	484.2 ± 0.4	503 ± 8	6700 ± 200	2.2 ± 0.3	2.6 ± 0.4	-1.6 ± 0.1
V57	508.5 ± 0.4	497 ± 8	6500 ± 150	3.0 ± 0.2	3.5 ± 0.3	-1.4 ± 0.1
V73	467.7 ± 0.8	495 ± 8	7300 ± 150	2.6 ± 0.2	3.4 ± 0.3	-1.6 ± 0.1
V83	464.9 ± 1.0	492 ± 8	7300 ± 150	2.7 ± 0.2	2.8 ± 0.2	-1.5 ± 0.1
94180	498.1 ± 0.3	498 ± 8	5600 ± 150	2.9 ± 0.3	2.2 ± 0.3	-1.3 ± 0.1

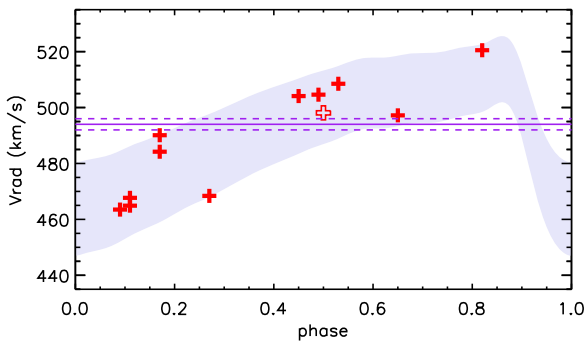


Figure 3. Measured instantaneous radial velocity for the sample stars (red crosses). The empty cross marks the RHB star at the arbitrary phase 0.5. The shaded area shows an ensemble of the velocity curves obtained with the template by Sesar (2012). The average cluster velocity and errors on the mean are shown with purple lines.

detailed list). Figure 8 shows several published iron abundance determinations for NGC 3201, and error bars display the standard deviations (σ) of the different samples. The solid and dashed purple lines show the average and 1σ dispersion of the entire sample, compared with our result. The data plotted in the figure show that the bulk of the iron abundances for NGC 3201 do agree within 1σ .

In particular, the most recent (ten years) estimates further suggest that NGC 3201 is a canonical metal-intermediate globular. Indeed, the average abundance for these recent works is $\langle [\text{Fe}/\text{H}] \rangle = -1.48 \pm 0.02$, $\sigma = 0.05$. Differences between the authors reflect their different approaches.

- The sample sizes vary by two orders of magnitude, from 2 (Gratton 1982) to 162 (Carretta et al. 2009a) stars, so that the final abundance might not be representative of the entire cluster in some cases.
- Different techniques are used to estimate the atmospheric parameters. Photometric or spectroscopic estimates of effective temperature and surface gravity are used, based on differential colors or on line intensities. Different techniques can lead to different results even on the same data sample.
- The cluster metallicity is estimated with different methods, using either spectroscopic or photometric techniques (ΔS : Smith & Manduca 1983; Q_{39} : Zinn & West 1984; EW: Gonzalez & Wallerstein 1998).

Most studies generally agree on the average NGC 3201 metallicity, but the possible existence of an intrinsic [Fe/H] spread within the cluster is not settled. The definition of spread can vary among the authors, so here we define as spread the standard deviation σ of the sample. Smith & Manduca (1983), Kraft & Ivans (2003) and Muñoz et al. (2013) found no evidence of variation in the iron content of the cluster. Carretta et al. (2009a) analyzed the largest sample of stars (162) in NGC 3201, and also found an internal metallicity spread of only 0.05 dex. On the other hand, Gonzalez & Wallerstein (1998) and Simmerer et al. (2013) reported an internal [Fe/H] spread in NGC 3201 of 0.14 and 0.1 dex respectively, with a difference as large as ~ 0.4 dex between the highest and the lowest metallicities of the cluster members. Their abundance analyses were based on large samples of cluster members (18 and 26 stars). However, different authors using the same spectra obtained different conclusions about the metallicity spread in NGC 3201. Covey et al. (2003) analyzed a sub-sample of the Gonzalez & Wallerstein (1998) spectra, supporting a spread in iron of ~ 0.14 dex when estimating the effective temperatures using spectroscopic diagnostics. However, the spread in iron decreased to ~ 0.08 dex when T_{eff} values were estimated with photometric diagnostics. A similar result was also obtained by Mucciarelli et al. (2015) using the Simmerer et al. (2013) spectra. Covey et al. and Mucciarelli et al. suggested that the spread in iron abundance shows up in spectroscopic analyses that do not properly take account for non-LTE effects.

The star-to-star scatter derived in our LTE analysis of NGC 3201 RR Lyrae stars is small, $\sigma \sim 0.14$, and is in accord with prior publications that assert that this cluster is monometallic.

4.2. α -elements: Mg, Ca, and Ti

The restricted wavelength coverage of our M2FS spectra limited the number of transitions for true α -elements to one each for Mg I and Ca I (Tables 3 and 7), not allowing a detailed analysis of these two elements. Although Ti is not a “pure” α -element because its dominant isotope is ^{48}Ti instead of ^{44}Ti , we included it in this group because its abundance at low metallicity usually mimics those of other α -elements. We measured up to 17 Ti I and Ti II lines per spectrum in the best cases, so Ti abundances are the most precise among the three α .

Table 3
Line List and Atomic Parameters

λ (Å)	Species	EP (eV)	$\log(gf)$ (dex)	λ (Å)	Species	EP (eV)	$\log(gf)$ (dex)	λ (Å)	Species	EP (eV)	$\log(gf)$ (dex)
4702.991	Mg I	4.346	-0.44	4690.138	Fe I	3.684	-1.68	5195.472	Fe I	4.217	0.02
5265.556	Ca I	2.521	-0.26	4728.546	Fe I	3.651	-1.28	5198.711	Fe I	2.221	-2.09
4670.407	Sc II	1.357	-0.58	4733.591	Fe I	1.484	-2.99	5215.181	Fe I	3.263	-0.86
5031.021	Sc II	1.357	-0.40	4736.773	Fe I	3.209	-0.67	5217.389	Fe I	3.209	-1.07
5239.813	Sc II	1.455	-0.77	4741.529	Fe I	2.829	-2.00	5232.940	Fe I	2.938	-0.19
5039.957	Ti I	0.021	-1.08	4745.800	Fe I	3.651	-1.25	5242.491	Fe I	3.632	-0.84
5064.653	Ti I	0.048	-0.94	4786.807	Fe I	3.015	-1.59	5243.776	Fe I	4.253	-1.15
5210.384	Ti I	0.048	-0.82	4788.757	Fe I	3.234	-1.81	5269.537	Fe I	0.858	-1.33
4708.663	Ti II	1.236	-2.35	4938.814	Fe I	2.873	-1.08	5292.597	Fe I	4.987	-0.03
4874.009	Ti II	3.092	-0.86	4939.687	Fe I	0.858	-3.25	5302.303	Fe I	3.281	-0.73
4911.194	Ti II	3.121	-0.64	4967.897	Fe I	4.188	-0.53	5324.179	Fe I	3.211	-0.11
5072.286	Ti II	3.121	-1.02	4973.102	Fe I	3.960	-0.69	4620.513	Fe II	2.828	-3.19
5129.156	Ti II	1.890	-1.34	4983.250	Fe I	4.151	-0.11	4731.439	Fe II	2.891	-3.10
5211.530	Ti II	2.588	-1.41	5001.864	Fe I	3.882	-0.01	4993.355	Fe II	2.807	-3.70
4600.749	Cr I	1.003	-1.25	5005.712	Fe I	3.884	-0.12	5197.568	Fe II	3.230	-2.05
4616.124	Cr I	0.982	-1.19	5014.943	Fe I	3.940	-0.18	5234.624	Fe II	3.221	-2.21
4626.173	Cr I	0.968	-1.33	5022.236	Fe I	3.984	-0.33	5264.801	Fe II	3.230	-3.23
4646.162	Cr I	1.029	-0.74	5044.211	Fe I	2.849	-2.15	5284.092	Fe II	2.891	-3.20
4651.291	Cr I	0.982	-1.46	5049.819	Fe I	2.277	-1.35	4648.652	Ni I	3.417	-0.09
4652.157	Cr I	1.003	-1.04	5074.748	Fe I	4.217	-0.20	4866.271	Ni I	3.536	-0.22
5296.691	Cr I	0.982	-1.36	5083.339	Fe I	0.957	-2.84	5035.362	Ni I	3.633	0.29
4616.629	Cr II	4.069	-1.29	5090.773	Fe I	4.253	-0.40	5081.107	Ni I	3.844	0.30
4634.073	Cr II	4.069	-0.98	5123.720	Fe I	1.010	-3.06	5084.089	Ni I	3.676	0.03
5237.329	Cr II	4.070	-1.16	5127.360	Fe I	0.914	-3.25	5099.927	Ni I	3.676	-0.10
5308.408	Cr II	4.068	-1.81	5131.468	Fe I	2.221	-2.52	5115.389	Ni I	3.831	-0.11
5313.563	Cr II	4.070	-1.65	5133.689	Fe I	4.175	0.36	5176.559	Ni I	3.895	-0.44
4598.117	Fe I	3.281	-1.57	5141.739	Fe I	2.422	-2.15	4722.153	Zn I	4.030	-0.33
4602.000	Fe I	1.607	-3.13	5150.840	Fe I	0.989	-3.04	4810.528	Zn I	4.078	-0.14
4602.941	Fe I	1.484	-2.21	5151.911	Fe I	1.010	-3.32	4883.684	Y II	1.083	0.07
4619.288	Fe I	3.600	-1.06	5159.058	Fe I	4.280	-0.82	4900.110	Y II	1.032	-0.09
4625.045	Fe I	3.239	-1.27	5162.273	Fe I	4.175	0.02	5087.420	Y II	1.083	-0.17
4678.846	Fe I	3.600	-0.68	5194.942	Fe I	1.556	-2.02	5200.413	Y II	0.992	-0.57

References. Sources: Mg I, NIST database (Kramida et al. 2018), Ca I, NIST, Sc II, NIST, Ti I (Lawler et al. 2013), Ti II (Wood et al. 2013), Cr I (Sobeck et al. 2007), Cr II (Lawler et al. 2017), Fe I (O’Brian et al. 1991; den Hartog et al. 2014; Ruffoni et al. 2014; Belmonte et al. 2017), Fe II, NIST, Ni I (Wood et al. 2014), Zn I, VALD database (Ryabchikova et al. 2015), Y II, NIST.

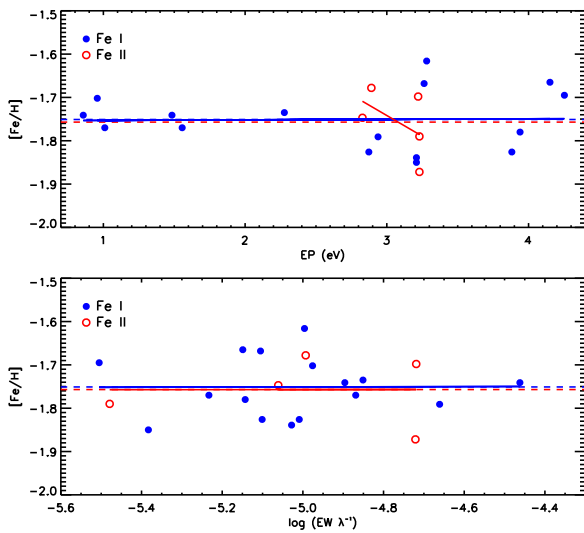


Figure 4. Individual iron line abundances for V26 in NGC 3201 as a function of excitation potential (top panel) and reduced equivalent width (bottom panel). Average abundances are shown with dashed lines. Linear fits of data points are shown with solid lines. Linear trends are minimized and neutral/ionized species are balanced to equilibrium.

The mean estimated abundances are $[\text{Mg}/\text{Fe}] = 0.13 \pm 0.05$, $[\text{Ca}/\text{Fe}] = 0.15 \pm 0.07$ and $[\text{Ti}/\text{Fe}] = 0.46 \pm 0.04$ (Table 7).

To further investigate the α -element abundances of NGC 3201 in the context of Galactic globulars, Figure 9 shows the comparison with measurements available in the literature (Pritzl et al. 2005; Carretta et al. 2009b, 2010, re-scaled to the solar abundances of Asplund et al. 2009). We performed a linear fit over the individual α -element abundances versus the iron content, in the range of metal–intermediate globulars ($-1.7 \lesssim [\text{Fe}/\text{H}] \lesssim -1.0$), to define the dispersion of the sample in the neighborhood of NGC 3201. In the context of Galactic globulars, Ti abundance agrees quite well within the dispersion (0.10 dex), whereas Mg and Ca, that have respectively the highest (0.13 dex) and the lowest (0.06 dex) dispersion, are located in the lower envelope of the observed abundance distribution, but still within 1σ .

The total abundance of α -elements (panel (d) in Figure 9) was estimated as the bi-weight mean of the abundances, with respect to iron, for the three individual elements. Bi-weight is a resistant and robust estimator of location, more insensitive to outliers than a simple mean or median, thanks to an iterative process (more details in Beers et al. 1990). To perform a solid comparison with similar estimates available in the literature, we

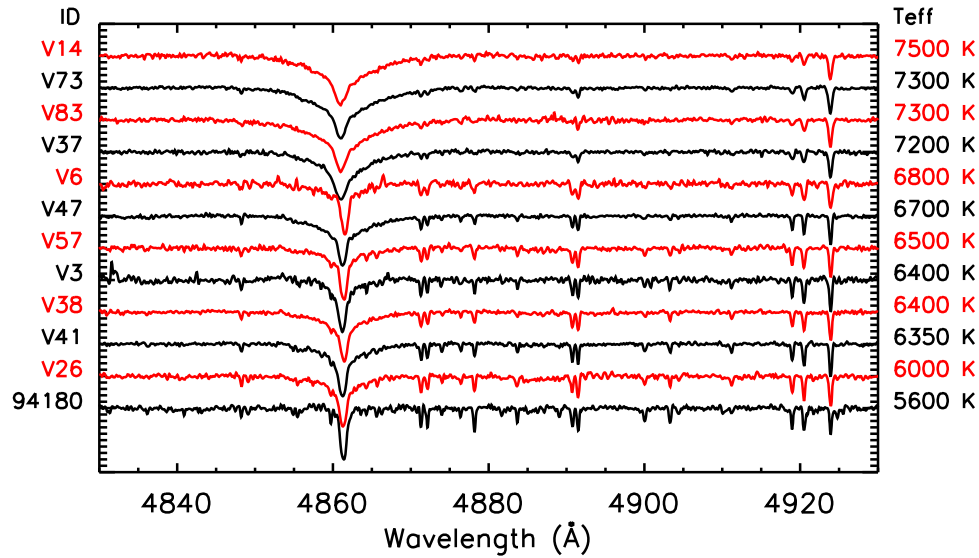


Figure 5. Portion of the observed M2FS spectra for the analyzed stars (listed on the left), sorted by estimated temperatures (listed on the right). The bottom spectrum is the cooler RHB star.

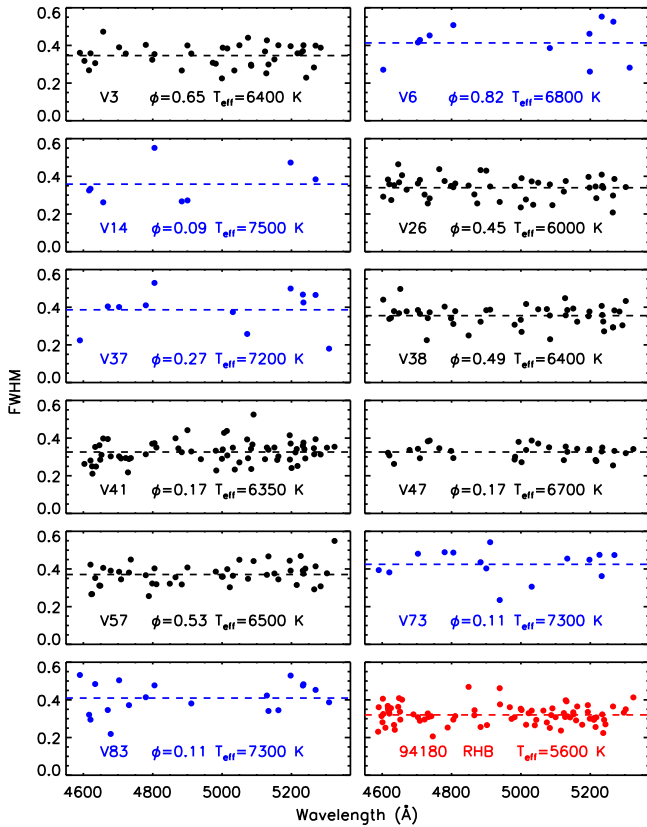


Figure 6. Individual FWHM of all the measured lines in the sample stars. Blue color highlights the warmest stars. Red color highlights the coolest, RHB star.

only included the sample stars for which we were able to measure the three quoted α -elements. We ended up with seven stars, and we found $[\alpha/\text{Fe}] = 0.37 \pm 0.04$ (see Table 7). On the other hand, if we estimate the bi-weight mean of the α -elements either as Ca+Ti or as Mg+Ti, we end up with $[\alpha/\text{Fe}] = 0.40 \pm 0.04$ and $[\alpha/\text{Fe}] = 0.39 \pm 0.03$, respectively, thus suggesting very similar enhancements. The comparison of the mean α -element abundance based on three elements is well in agreement with similar abundances for

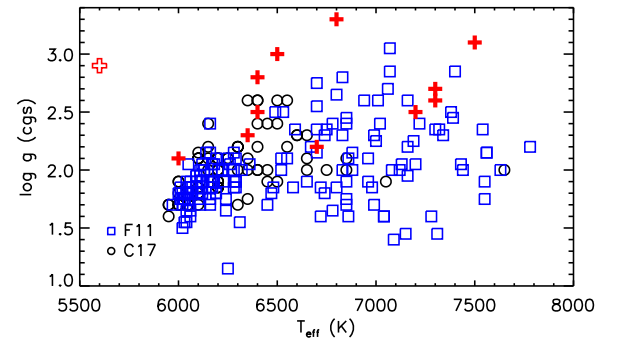


Figure 7. T_{eff} vs. $\log g$ for the stars in our sample (RRLs: filled red crosses; RHB: empty red cross) and a sample of field RRLs available in the literature (F11: For et al. 2011; C17: Chadid et al. 2017).

Table 4
Errors on Iron Abundances Associated with Errors on the Parameter Estimates

Species	ΔT_{eff} (100 K)	$\Delta \log g$ (0.3 dex)	$\Delta \xi_{\text{turb}}$ (0.5 km s ⁻¹)	σ_{tot}
$\Delta[\text{Fe I}/\text{H}]$	0.07	0.01	0.04	0.08
$\Delta[\text{Fe II}/\text{H}]$	0.02	0.10	0.06	0.12

Table 5
Iron Abundances and Number of Lines for Each Ionization State

ID	[Fe I/H]	n	[Fe II/H]	n	[Fe/H]
V3	-1.37 ± 0.05	16	-1.36 ± 0.03	5	-1.37 ± 0.03
V6	-1.18 ± 0.04	3	-1.22	1	-1.19 ± 0.03
V14	-1.57	1	-1.50 ± 0.16	2	-1.53 ± 0.09
V26	-1.75 ± 0.02	16	-1.76 ± 0.03	5	-1.75 ± 0.02
V37	-1.49 ± 0.06	2	-1.52 ± 0.04	2	-1.51 ± 0.03
V38	-1.48 ± 0.04	18	-1.49 ± 0.04	5	-1.48 ± 0.03
V41	-1.50 ± 0.03	28	-1.48 ± 0.04	6	-1.50 ± 0.03
V47	-1.60 ± 0.03	15	-1.59 ± 0.08	5	-1.60 ± 0.03
V57	-1.35 ± 0.04	20	-1.36 ± 0.05	5	-1.35 ± 0.03
V73	-1.55 ± 0.03	4	-1.55 ± 0.10	2	-1.55 ± 0.03
V83	-1.48 ± 0.08	5	-1.41 ± 0.10	4	-1.45 ± 0.06
94180	-1.33 ± 0.03	37	-1.32 ± 0.07	3	-1.33 ± 0.03
NGC 3201	-1.47 ± 0.04		-1.46 ± 0.04		-1.47 ± 0.04

Table 6
Iron Abundances and Number of Analyzed Stars in NGC 3201 from the Literature

[Fe/H]	σ	n	References ^a
-1.40 ± 0.06	Zinn (1980)
-1.40 ± 0.2	...	26	da Costa et al. (1981)
-1.19 ± 0.05	0.02	2	Gratton (1982)
-0.95 ± 0.2	0.03	4	Pilachowski et al. (1983)
-1.33 ± 0.05	0.15	9	Smith & Manduca (1983)
-1.61 ± 0.12	Zinn & West (1984)
-1.34 ± 0.05	0.13	3	Gratton & Ortolani (1989)
-1.21 ± 0.05	0.09	3	Carretta & Gratton (1997)
-1.44 ± 0.03	0.14	18	Gonzalez & Wallerstein (1998)
-1.39 ± 0.06	0.08	5	Covey et al. (2003)
-1.54 ± 0.10	0.09	13	Kraft & Ivans (2003)
-1.50 ± 0.02	0.05	162	Carretta et al. (2009a)
-1.53 ± 0.01	0.04	8	Muñoz et al. (2013)
-1.48 ± 0.02	0.1	26	Simmerer et al. (2013)
-1.42 ± 0.02	0.06	21	Mucciarelli et al. (2015)

Note.

^a Scaled to Asplund et al. (2009).

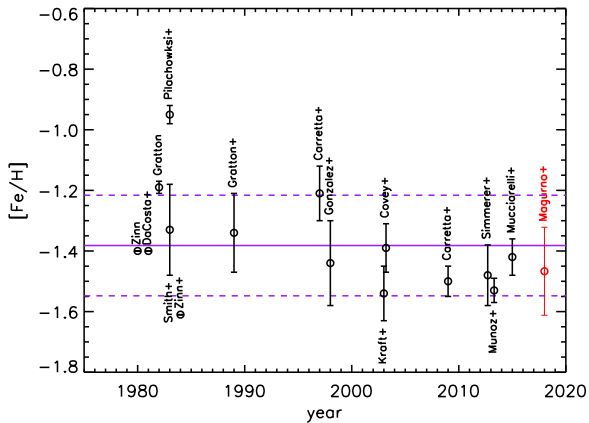


Figure 8. Determination of [Fe/H] for NGC 3201 from the literature (Zinn 1980; da Costa et al. 1981; Gratton 1982; Pilachowski et al. 1983; Smith & Manduca 1983; Zinn & West 1984; Gratton & Ortolani 1989; Carretta & Gratton 1997; Gonzalez & Wallerstein 1998; Covey et al. 2003; Kraft & Ivans 2003; Carretta et al. 2009a; Muñoz et al. 2013; Simmerer et al. 2013; Mucciarelli et al. 2015, see also Table 6). Error bars show the intrinsic dispersions. The sample mean and 1 dispersion are shown with purple lines.

Galactic globular clusters available in the literature (see Figure 9). Indeed, the mean α -element abundances for metal-intermediate globulars ($-1.7 \lesssim [\text{Fe}/\text{H}] \lesssim -1.0$) range from ~ 0.23 (NGC 6205/M13, NGC 6254/M10) to ~ 0.45 dex (NGC 1904/M79), with a dispersion of 0.06 dex.¹⁸

To further investigate the possible differences between field and cluster RR Lyrae, we compared the current α -elements abundances with similar ones for field RR Lyrae. Figure 10 shows the comparison with 147 field RRLs (96 objects, see details in Table 10) for which the abundances are based on high-resolution spectra. They are marked with different

¹⁸ We neglected the two extreme clusters Rup 106 ($[\text{Fe}/\text{H}] = -1.36$, $[\alpha/\text{Fe}] \sim 0$) and NGC 6362 ($[\text{Fe}/\text{H}] = -1.04$, $[\alpha/\text{Fe}] \sim 0.56$). Solid evidence based on metallicity distribution and on the absolute age suggest that the former one was accreted (Villanova et al. 2013). The α -elements abundance of the latter is only based on two stars (Gratton 1987). However, more recent estimates based on a larger sample (Massari et al. 2017) suggest $[\text{Fe}/\text{H}] = -1.07$ and $[\alpha/\text{Fe}] = 0.37$ for NGC 6362, similar to the other metal-intermediate globulars.

symbols and colors and they have been re-scaled to the same solar abundances (Asplund et al. 2009). We selected the stars in common among the different spectroscopic samples to estimate the standard deviation in iron and α -element abundances as representative of the individual star errors (see the black error bars plotted in the bottom left corners of the figure). The range in iron abundance covered by field RRLs is similar to the globular iron abundances, with a slight overdensity of stars in the metal-intermediate range ($-1.7 \lesssim [\text{Fe}/\text{H}] \lesssim -1.0$). We found that Mg is confirmed to have the highest dispersion (0.14 dex). As for globulars, our results for NGC 3201 show a limited enhancement of Mg compared with RRLs of similar iron content. The other two α -elements (Ca, Ti) have smaller standard deviations, both ~ 0.08 dex. The Ca abundance is once again slightly under-enhanced, but within the intrinsic dispersion. On the other hand, the Ti abundance of RRLs in NGC 3201 seems to be, at fixed iron content, overenhanced when compared with field RRLs. The under- and over-enhancements of Mg–Ca and Ti mostly balance each other when considering the $[\alpha/\text{Fe}]$ ratios, so that NGC 3201 is in agreement with field RRLs of similar iron content, as showed in the panel (d) of Figure 10.

To constrain on a more quantitative basis the comparison between field and cluster RR Lyrae with field Halo stars we performed an analytical fit of $[\alpha/\text{Fe}]$ versus $[\text{Fe}/\text{H}]$ for both field RRLs and Galactic globulars. Note that, for these two subsamples, we have solid reasons to believe that their age is similar and ≥ 10 Gyrs. The fit was performed over the range in metallicity $-2.5 < [\text{Fe}/\text{H}] < 0.0$, as the sampling of the more metal-poor regime is limited. We adopted a log-normal distribution and we found

$$[\alpha/\text{Fe}] = H \exp \left[\ln(2) \frac{X^2}{A^2} \right] \quad (1)$$

with

$$X = \ln \left[1 + \frac{2A([\text{Fe}/\text{H}] - [\text{Fe}/\text{H}]_0)}{\sigma} \right], \quad (2)$$

where H (scale height) = 0.359438, representing the $[\alpha/\text{Fe}]$ abundance for very metal-poor ($[\text{Fe}/\text{H}] \lesssim -2$) stars, A (asymmetry) = -1.74038 , $[\text{Fe}/\text{H}]_0 = -2.56024$ and $\sigma = 8.98116$. The top panel of Figure 11 shows the analytical fit (blue line), together with the quoted subsamples. The bottom panel of the same figure shows the comparison of the quoted analytical fit, extrapolated down to $[\text{Fe}/\text{H}] = -4$ (dashed blue line), with the mean $[\alpha/\text{Fe}]$ abundance for NGC 3201 (red cross), the kinematically selected field Halo giants (black dots) collected by Frebel (2010) and field Halo blue (blue squares, BHB) and red (orange squares, RHB) HB stars collected by For & Sneden (2010). Interestingly enough, the different samples do agree within 1σ , thus suggesting a very similar chemical enrichment history even though they cover different ranges in iron content and in Galactocentric distances. This finding further supports a common old ($t \geq 10$ Gyr) age for field RG and HB stars.

4.3. Iron-peak Elements: Sc, Cr, Ni, and Zn

Iron-peak elements are defined as those with $Z = 21\text{--}30$. We measured spectral lines of four iron-peak elements: Sc, Cr, Ni, and Zn (see Table 8 for details). Chromium is the most represented

Table 7
 α -elements Abundances and Number of Lines

ID	[Mg/Fe]	n	[Ca/Fe]	n	[Ti/Fe]	n	[α /Fe]
V3	0.09	1	0.34 ± 0.07	10	...
V6	-0.09	1	-0.13	1	0.61 ± 0.18	2	0.25 ± 0.27
V14	0.76 ± 0.12	2	...
V26	0.20	1	0.27	1	0.43 ± 0.04	13	0.40 ± 0.10
V37	0.15	1	0.35 ± 0.08	4	...
V38	0.24	1	0.14	1	0.35 ± 0.03	9	0.32 ± 0.06
V41	0.09	1	0.22	1	0.39 ± 0.03	16	0.37 ± 0.09
V47	0.31	1	0.11	1	0.26 ± 0.02	7	0.25 ± 0.04
V57	0.13	1	0.01	1	0.60 ± 0.04	12	0.54 ± 0.13
V73	0.30	1	0.49 ± 0.04	5	...
V83	0.22	1	0.49 ± 0.11	5	...
94180	-0.19	1	0.45	1	0.46 ± 0.08	17	0.43 ± 0.20
NGC 3201	0.13 ± 0.05		0.15 ± 0.07		0.46 ± 0.04		0.37 ± 0.04

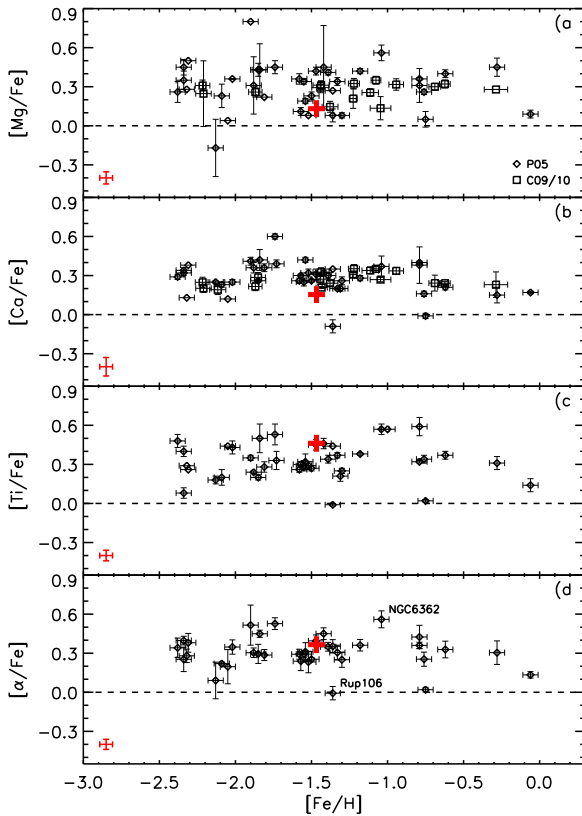


Figure 9. α -elements vs. iron abundances of Galactic globular clusters (P05 = Pritzl et al. 2005; C09/10 = Carretta et al. 2009b, 2010). The red cross, with red error bar in the bottom left corner, shows our analysis of NGC 3201.

element in our sample, as it was measured in 11 out of 12 stars, with up to 10 lines in the RHB star. The other three elements (Sc, Ni, and Zn) were observed in only a half of the current sample with a limited number of lines. Our derived mean abundances are $\langle [\text{Sc}/\text{Fe}] \rangle = 0.14 \pm 0.06$, $\langle [\text{Cr}/\text{Fe}] \rangle = 0.12 \pm 0.05$, $\langle [\text{Ni}/\text{Fe}] \rangle = -0.02 \pm 0.04$ and $\langle [\text{Zn}/\text{Fe}] \rangle = 0.22 \pm 0.06$.

Figure 12 shows these abundances and those for field Halo RRLs (see details in Table 11). The Fe-group abundance ratios in NGC 3201 generally agree with those of the other RRLs. Nickel abundances deserve some comment. Our $[\text{Ni}/\text{Fe}]$ values agree with most of the previous studies, but the abundances by

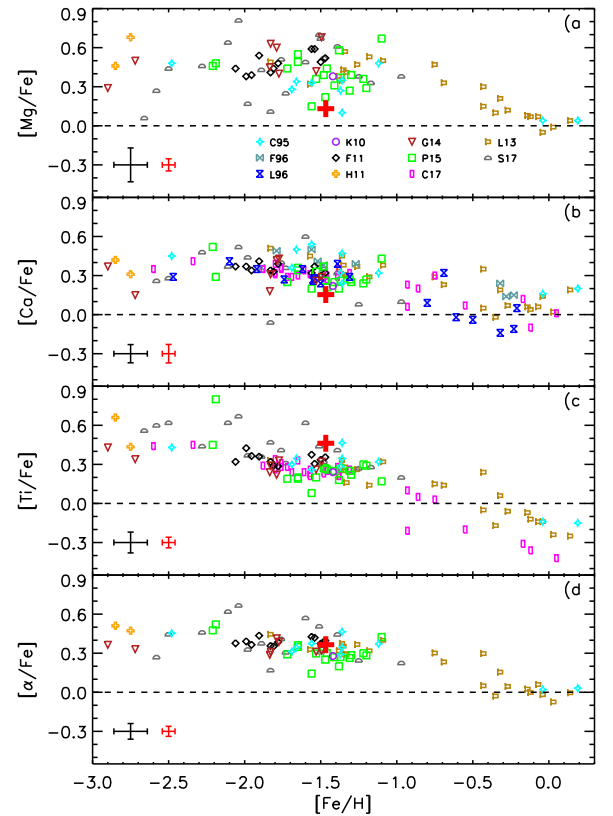


Figure 10. α -elements vs. iron abundances by high-resolution spectroscopy of field Halo RRLs (C95: Clementini et al. 1995; F96: Fernley & Barnes 1996; L96: Lambert et al. 1996; K10: Kolenberg et al. 2010a; F11: For et al. 2011; H11: Hansen et al. 2011; L13: Liu et al. 2013; G14: Govea et al. 2014; P15: Pancino et al. 2015; C17: Chadid et al. 2017; S17: Sneden et al. 2017). The black error bars on bottom left corner show the mean individual errors. The red cross, with red error bar in the bottom left corner, shows our analysis of NGC 3201.

For et al. (2011) and by Govea et al. (2014) appear to be enhanced by ~ 0.5 dex. For et al. (2011) noted that the phase to phase scatter in Ni abundances, for which they only measured a couple of lines, should be treated with caution. This scatter can be seen in their Figures 23 and 26. Govea et al. (2014) measured only one Ni line and in a single phase for each star, so their estimates have larger uncertainties. We conclude that

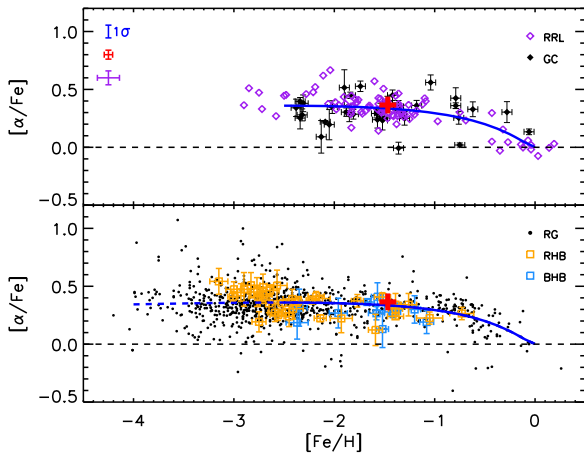


Figure 11. Top panel: α -elements (Mg+Ca+Ti) vs. iron abundances of Galactic globulars (filled black diamonds) and field Halo RRLs (open purple diamonds, typical error bar is shown on top left corner). The two samples are the same as in panels (d) of Figures 9–10. The red cross, with red error bar in the top left corner, shows our analysis of NGC 3201. The solid blue line shows the log-normal fit of the two joint samples, with the 1σ dispersion shown by the blue bar in the top left corner. Bottom panel: comparison of field Halo giants (black dots, Frebel 2010) and RHB–BHB field stars (orange–blue squares, For & Sneden 2010). The red cross shows our analysis of NGC 3201. The solid blue line shows the log-normal fit of the joint samples of field Halo RRLs and Galactic globulars as in the upper panel. The dashed blue line shows an extrapolation of the fit toward lower iron abundances.

our Fe-group abundances are in agreement with other stellar samples in this metallicity regime.

In Figure 13, we show our Fe-group abundances and those of field Halo giants collected by Frebel (2010) and Halo RHB–BHB stars by For & Sneden (2010). All the elements in NGC 3201 are in good agreement with other stars in the intermediate metallicity regime. This suggests once again that field Halo RGs, field HBs (RHB, RRL, BHB) and globular clusters share similar chemical enrichments.

4.4. *s*-process Element: Yttrium

The slow neutron-capture process (*s*-process), in which timescales for capture of free neutrons are longer than timescales of β -decays, has dominated the production of yttrium in solar system material. However, the *s*-process fractional dominance over the *r*-process (rapid neutron capture) that produced solar Y is still an open question. Simmerer et al. (2004) estimated a fraction of $\sim 72\%$, whereas Arlandini et al. (1999) estimated much higher values of $\sim 92\%$ – 100% .

Within the M2FS spectral range, we identified five potentially useful Y II lines, and measured up to four EWs in nine out of our twelve stars (see Table 9). From these, we estimated an average abundance for NGC 3201 of $\langle [Y/Fe] \rangle = 0.08 \pm 0.05$. Figure 14 shows the comparison of this result and average Y abundances of other Galactic globulars (Pritzl et al. 2005). The cluster-to-cluster scatter in $[Y/Fe]$ appears to be large, but this could simply reflect study-to-study differences in the Pritzl et al. (2005) compilation. Relatively metal-rich clusters show a small dispersion and an average $[Y/Fe]$ abundance close to solar, with the exception of the outer Halo cluster Pal 12. The peculiarity of this cluster is not surprising, since there are photometric and spectroscopic reasons to believe that Pal 12 is an accreted cluster (Musella et al. 2018, and references therein). Clusters

with $[Fe/H] \lesssim -1.8$ often exhibit sub-solar $[Y/Fe]$ values, but the scatter is still large. Field Halo RRLs yield similar $[Y/Fe]$ results in the metal-intermediate ($-1.7 \lesssim [Fe/H] \lesssim -1$) regime (Figure 15). Comparison of the data for globular clusters and field stars shows mostly that a future study is needed to bring coherence to $[Y/Fe]$ abundance trends with metallicity.

Of special interest is the behavior of $[Y/Fe]$ in the metal-rich ($[Fe/H] \gtrsim -1.0$) regime. Field RRLs shows a severe depletion of Y ($[Y/Fe] = -0.48 \pm 0.15$; Figure 15), but ones in clusters do not (Figure 14). The metal-rich RRLs mainly come from the data set collected by Liu et al. (2013), with the exception of two stars provided by Clementini et al. (1995). The two stars by Clementini et al. are also in the data set by Liu et al., with very similar derived abundances, excluding the possibility of systematics in one of the two samples. Considerations about their radial velocities suggest that these RRLs are candidate members of the Galactic disk, not the Halo (Liu et al. 2013). To further investigate RRLs in the metal-rich regime, we compared their abundances with Halo stars. In Figure 16 we plot $[Y/Fe]$ ratios versus metallicity for various samples of stars. In the metal-poor domain ($[Fe/H] \lesssim -1.0$), the field RRLs show agreement, on average, with other field Halo stars, namely RG and HB stars. On the contrary, the metal-rich ($[Fe/H] \gtrsim -1.0$) tail of RRLs is clearly depleted in Y when compared with slightly more metal-poor ($[Fe/H] \sim -1.0$) field Halo stars and with Disk dwarfs of similar metallicities (Reddy et al. 2006). These results, coupled with the radial velocity considerations by Liu et al. (2013), suggest that they may be candidate Bulge members.

In Figure 16 we also include $[Y/Fe]$ predicted trends from evolutionary prescriptions based on Asymptotic Giant Branch models available on the FRUITY¹⁹ database (Cristallo et al. 2011, 2015). Blue lines in the figure show predicted values for three different stellar masses (see labelled values). Unfortunately, for masses $\leq 1.1 M_{\odot}$, as the RRLs have, the accounted models are not available because they do not experience the third dredge up and, therefore, do not show a significant chemical enrichment of the environment. However, the theoretical predictions for the less massive available stars show a rapid decrease in Y abundance for $[Fe/H] \gtrsim -0.45$, suggesting that we are moving in the right direction.

5. Conclusion and Final Remarks

We performed the first high-resolution, high SNR, large spectroscopic investigation of RRLs in NGC 3201. Our independent analysis confirmed many previous results on the cluster using non-variable stars. Our derived average metallicity of the cluster, $\langle [Fe/H] \rangle = -1.47 \pm 0.04$, is in general accord with recent studies, and we confirm that NGC 3201 is a homogeneous, monometallic cluster.

A limited dispersion was also observed for three different groups of elements: the light α -elements Mg–Ca–Ti, the iron-peak elements Sc–Cr–Ni–Zn and the *s*-process element Y. The α -elements were found to be enhanced with respect to the Sun, as expected for old ($t \geq 10$ Gyr) stellar structures, with abundances comparable to other known globular clusters and field stars of similar metallicity. In particular, the agreement was found not only with HB stars (RHB, RRL, BHB) as the ones in our sample, but in general with variable and

¹⁹ <http://fruity.ia-teramo.inaf.it/>

Table 8
Iron-peak Elements Abundances and Number of Lines

ID	[Sc/Fe]	<i>n</i>	[Cr/Fe]	<i>n</i>	[Ni/Fe]	<i>n</i>	[Zn/Fe]	<i>n</i>
V3	0.06 ± 0.14	3	-0.04 ± 0.11	2	0.42	1
V6	0.47	1
V14	0.27	1
V26	0.20 ± 0.02	2	0.19 ± 0.02	5	-0.06 ± 0.12	2	0.35 ± 0.08	2
V37	0.12 ± 0.00	2	0.20	1
V38	-0.04 ± 0.16	2	-0.05 ± 0.11	3	-0.10 ± 0.07	2	0.19	1
V41	0.15 ± 0.11	3	0.00 ± 0.02	5	-0.11 ± 0.09	2	0.23 ± 0.06	2
V47	0.05	1	-0.15 ± 0.10	2	0.17	1
V57	0.21 ± 0.10	2	0.02 ± 0.02	2	0.04	1	0.13	1
V73	-0.17	1
V83	0.53	1	0.25 ± 0.13	3
94180	0.23 ± 0.04	2	0.04 ± 0.05	9	-0.04 ± 0.04	5	-0.02 ± 0.12	2
NGC 3201	0.14 ± 0.06		0.12 ± 0.05		-0.02 ± 0.04		0.22 ± 0.06	

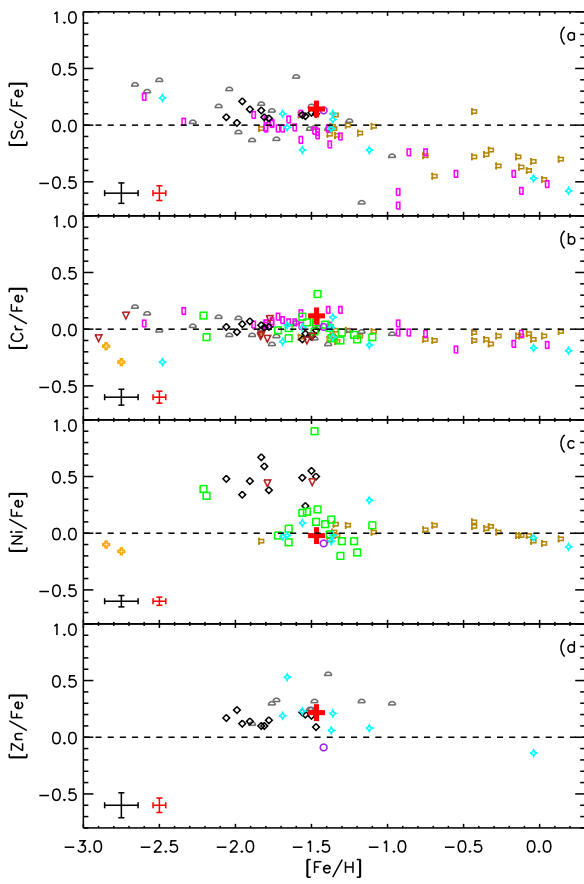


Figure 12. Iron-peak elements vs. iron abundance by high-resolution spectroscopy of field Halo RRLs (same symbols as in Figure 10). The black error bars on bottom left corner show the mean individual errors. The red cross, with red error bar in the bottom left corner, shows our analysis of NGC 3201.

non-variable field Halo stars. We found $\langle [\text{Mg}/\text{Fe}] \rangle = 0.13 \pm 0.05$, $\langle [\text{Ca}/\text{Fe}] \rangle = 0.15 \pm 0.07$ and $\langle [\text{Ti}/\text{Fe}] \rangle = 0.46 \pm 0.04$. The same homogeneity was observed for the iron-peak and *s*-process elements, whose abundance ratios are close to solar and similar to other metal-intermediate ($-1.7 \lesssim [\text{Fe}/\text{H}] \lesssim -1.0$) globulars and field Halo stars. These results suggests

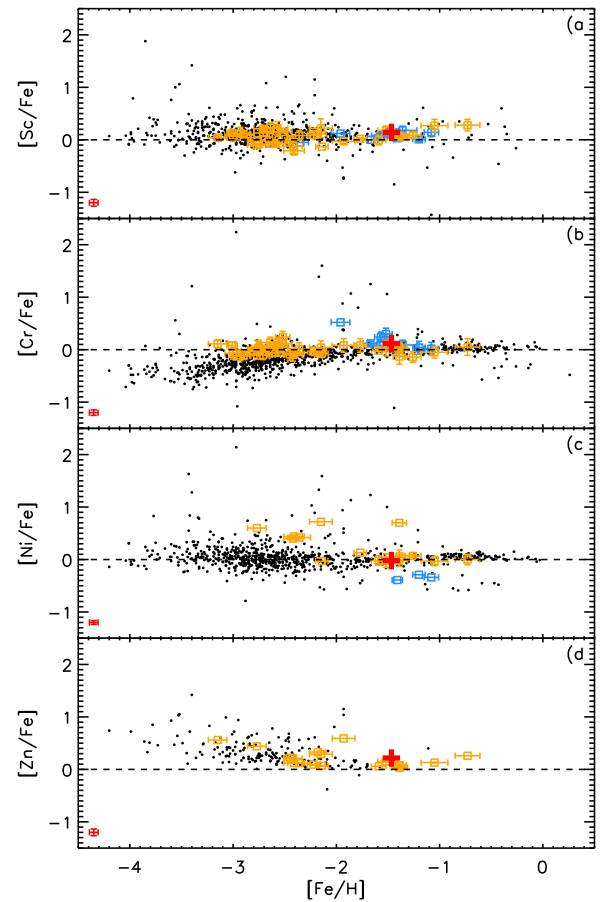


Figure 13. Iron-peak elements vs. iron abundance of field Halo giants and RHB-BHB field stars (same symbols as in Figure 11). The red cross, with red error bar in the bottom left corner, shows our analysis of NGC 3201.

similar enrichment histories for all the analyzed Halo components with similar metallicity to NGC 3201.

The cluster radial velocity was estimated as $494 \pm 2 \pm 8 \text{ km s}^{-1}$, where the two errors are the error on the mean and the standard deviation, respectively. The use of a template to obtain a radial velocity curve from a single-epoch velocity measurement of a RRL star is a very promising approach.

Table 9
Yttrium Abundances and Number of Lines

ID	[Y/Fe]	<i>n</i>
V3	-0.01 ± 0.15	2
V6
V14	0.28 ± 0.10	2
V26	0.24 ± 0.01	2
V37
V38	-0.14 ± 0.09	2
V41	0.04 ± 0.06	4
V47	-0.17 ± 0.07	2
V57	0.15 ± 0.11	2
V73	0.15 ± 0.04	2
V83
94180	0.17 ± 0.14	3
NGC 3201	0.08 ± 0.05	

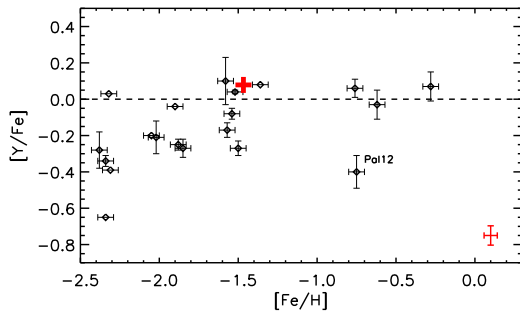


Figure 14. Yttrium vs. iron abundance of globular clusters (Pritzl et al. 2005). The red cross, with red error bar in the bottom right corner, shows our analysis of NGC 3201.

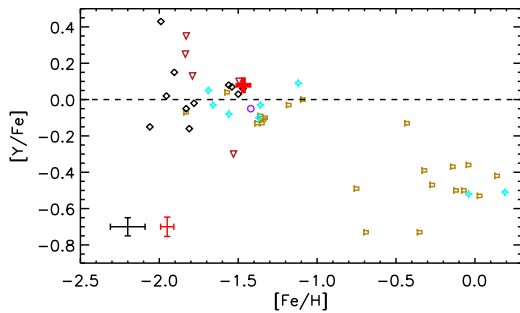


Figure 15. Yttrium vs. iron abundance by high-resolution spectroscopy of field Halo RRLs (symbols as in Figure 10; see also Table 11). The black error bar on bottom left corner shows the mean individual error. The red cross, with red error bar in the bottom left corner, shows our analysis of NGC 3201.

However, to obtain more precise results it is necessary a good photometric data set, almost coeval to the spectroscopic data. The goodness of this approach is further supported by the homogeneity of the average template velocities of the RRLs in our sample and the non-variable star instantaneous velocity.

The results obtained with this work on NGC 3201 strongly supports the capabilities of M2FS at Magellan as a high quality instrument for abundance investigations, even in crowded

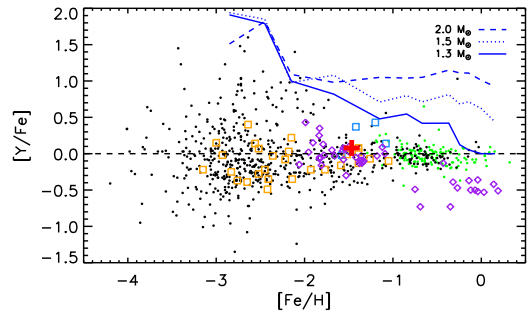


Figure 16. Yttrium vs. iron abundances of field Halo giants (black dots, Frebel 2010), RHB-BHB field stars (orange-blue squares, For & Sneden 2010), Thin-thick disk stars (green dots, Reddy et al. 2006) and high-resolution spectroscopic RRLs (purple diamonds, same sample as in Figure 15). The red cross shows our analysis of NGC 3201. The blue lines show theoretical predictions for different solar masses, based on the FRUITY database (Cristallo et al. 2011, 2015).

fields such as a globular cluster. This work on NGC 3201 is opening the path to a forthcoming analysis on the more complex Globular cluster ω Cen, which is known to have an intrinsic metallicity spread, for which we already collected M2FS spectra of ~ 140 RRLs.

C.S. was partially supported by NSF grant AST-1616040, and by the Rex G Baker, Jr. Endowment at the University of Texas. C.S. also thanks the Dipartimento di Fisica—Università di Roma Tor Vergata for a Visiting Scholar grant and INAF—Osservatorio Astronomico di Roma for his support during his stay. M.M. was partially supported by NSF grant AST-1714534. It is a real pleasure to thank P.B. Stetson for sending us in advance of publication optical photometry for the variables included in this investigation. We also thank Ivan Ferraro and Giacinto Iannicola of the INAF—Osservatorio Astronomico di Roma for the help in computing analytical relations for α -element abundances in the Halo. Moreover, many thanks to Sergio Cristallo for the fruitful discussion about r - and s - process elements and for sending us the models about Yttrium abundances computed with the FRUITY database. Finally, we thank the reviewer for the precise notes and the useful suggestions to improve our work.

This work has made use of the VALD database (<http://vald.astro.univie.ac.at/~vald3/php/vald.php>), operated at Uppsala University, the Institute of Astronomy RAS in Moscow, and the University of Vienna.

Appendix High-resolution Spectroscopy in the Literature

Several authors estimated abundances for RR Lyrae stars using high-resolution ($R > 20,000$) spectroscopy. We collected here the abundances of Fe, Mg, Ca, and Ti (Table 10), and Sc, Cr, Ni, Zn, and Y (Table 11) for 147 field RRLs (96 objects). The abundances have been estimated by 10 different authors in the period from 1995 to 2017. They are all scaled to the solar reference by Asplund et al. (2009).

Table 10
Iron and α -elements Abundances of High-resolution RRLs

ID	[Fe/H]	[Mg/Fe]	[Ca/Fe]	[Ti/Fe]	References
AA Aql	-0.32	0.21	0.19	0.06	L13
AE Dra	-1.46	0.44	0.21	0.26	P15
AN Ser	0.05	...	0.01	-0.42	C17
AO Peg	-1.26	0.47	0.37	0.26	L13
AR Per	-0.23	...	-0.11	...	L96
AR Per	-0.28	...	0.14	...	F96
AR Per	-0.29	A18
AS Vir	-1.57	...	0.31	0.21	C17

References. C95: Clementini et al. (1995), L96: Lambert et al. (1996), K10: Kolenberg et al. (2010a), F11: For et al. (2011), H11: Hansen et al. (2011), L13: Liu et al. (2013), G14: Govea et al. (2014), P15: Pancino et al. (2015), C17: Chadid et al. (2017), S17: Sneden et al. (2017). All scaled to Asplund et al. (2009).

(This table is available in its entirety in machine-readable form.)


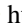






Table 11
Iron-peak and s -process Elements Abundances of High-resolution RRLs

ID	[Sc/Fe]	[Cr/Fe]	[Ni/Fe]	[Zn/Fe]	[Y/Fe]	References
AA Aql	-0.22	-0.13	0.06	...	-0.39	L13
AE Dra	...	0.31	0.21	P15
AN Ser	-0.52	-0.14	C17
AO Peg	0.00	-0.01	0.07	L13
AS Vir	-0.13	0.14	C17
AS Vir	0.06	0.02	0.38	0.15	-0.02	F11
ASAS J081933-2358.2	...	-0.08	G14
ASAS J085254-0300.3	0.17	-0.05	...	0.25	...	S17

References. C95: Clementini et al. (1995), K10: Kolenberg et al. (2010a), F11: For et al. (2011), H11: Hansen et al. (2011), L13: Liu et al. (2013), G14: Govea et al. (2014), P15: Pancino et al. (2015), C17: Chadid et al. (2017), S17: Sneden et al. (2017). All scaled to Asplund et al. (2009).

(This table is available in its entirety in machine-readable form.)

ORCID iDs

D. Magurno  <https://orcid.org/0000-0001-5479-5062>
 C. Sneden  <https://orcid.org/0000-0002-3456-5929>
 V. F. Braga  <https://orcid.org/0000-0001-7511-2830>
 G. Bono  <https://orcid.org/0000-0002-4896-8841>
 M. Dall'Ora  <https://orcid.org/0000-0001-8209-0449>
 M. Marengo  <https://orcid.org/0000-0001-9910-9230>
 M. Monelli  <https://orcid.org/0000-0001-5292-6380>
 J. R. Neeley  <https://orcid.org/0000-0002-8894-836X>

References

Adamow, M. M. 2017, in AAS Meeting Abstracts, 230, 216.07
 Andrievsky, S., Wallerstein, G., Korotin, S., et al. 2018, *PASP*, 130, 024201
 Arlandini, C., Käppeler, F., Wisshak, K., et al. 1999, *ApJ*, 525, 886
 Asplund, M., Grevesse, N., Sauval, A. J., & Scott, P. 2009, *ARA&A*, 47, 481
 Baade, W. 1958, *AJ*, 63, 207
 Baade, W., & Swope, H. H. 1955, *AJ*, 60, 151
 Beers, T. C., Flynn, K., & Gebhardt, K. 1990, *AJ*, 100, 32
 Belmonte, M. T., Pickering, J. C., Ruffoni, M. P., et al. 2017, *ApJ*, 848, 125
 Benkő, J. M., Plachy, E., Szabó, R., Molnár, L., & Kolláth, Z. 2014, *ApJS*, 213, 31
 Bono, G., Caputo, F., Castellani, V., et al. 2003, *MNRAS*, 344, 1097
 Bono, G., Caputo, F., & di Criscienzo, M. 2007, *A&A*, 476, 779
 Bono, G., Caputo, F., & Stellingwerf, R. F. 1994, *ApJL*, 432, L51
 Bono, G., & Stellingwerf, R. F. 1994, *ApJS*, 93, 233
 Braga, V. F., Dall'Ora, M., Bono, G., et al. 2015, *ApJ*, 799, 165
 Braga, V. F., Stetson, P. B., Bono, G., et al. 2018, *AJ*, 155, 137
 Buchler, J. R., & Kolláth, Z. 2011, *ApJ*, 731, 24

Caputo, F. 1997, *MNRAS*, 284, 994
 Carretta, E., Bragaglia, A., Gratton, R., et al. 2010, *ApJL*, 712, L21
 Carretta, E., Bragaglia, A., Gratton, R., D'Orazi, V., & Lucatello, S. 2009a, *A&A*, 508, 695
 Carretta, E., Bragaglia, A., Gratton, R., & Lucatello, S. 2009b, *A&A*, 505, 139
 Carretta, E., & Gratton, R. G. 1997, *A&AS*, 121, 95
 Castelli, F., & Kurucz, R. L. 2003, in *IAU Symp. 210, Modelling of Stellar Atmospheres*, ed. N. Piskunov, W. W. Weiss, & D. F. Gray (San Francisco, CA: ASP), A20
 Chadid, M., Sneden, C., & Preston, G. W. 2017, *ApJ*, 835, 187
 Clementini, G., Carretta, E., Gratton, R., et al. 1995, *AJ*, 110, 2319
 Clementini, G., Federici, L., Corsi, C., et al. 2001, *ApJL*, 559, L109
 Coppola, G., Stetson, P. B., Marconi, M., et al. 2013, *ApJ*, 775, 6
 Covey, K. R., Wallerstein, G., Gonzalez, G., Vanture, A. D., & Suntzeff, N. B. 2003, *PASP*, 115, 819
 Cristallo, S., Piersanti, L., Straniero, O., et al. 2011, *ApJS*, 197, 17
 Cristallo, S., Straniero, O., Piersanti, L., & Gobrecht, D. 2015, *ApJS*, 219, 40
 da Costa, G. S., Frogel, J. A., & Cohen, J. G. 1981, *ApJ*, 248, 612
 da Costa, G. S., Rejkuba, M., Jerjen, H., & Grebel, E. K. 2010, *ApJL*, 708, L121
 den Hartog, E. A., Ruffoni, M. P., Lawler, J. E., et al. 2014, *ApJS*, 215, 23
 Drake, A. J., Catelan, M., Djorgovski, S. G., et al. 2013, *ApJ*, 763, 32
 Fernley, J., & Barnes, T. G. 1996, *A&A*, 312, 957
 Ferraro, F. R., Mucciarelli, A., Lanzoni, B., et al. 2018, *ApJ*, 860, 50
 Fiorentino, G., Bono, G., Monelli, M., et al. 2015, *ApJL*, 798, L12
 For, B.-Q., & Sneden, C. 2010, *AJ*, 140, 1694
 For, B.-Q., Sneden, C., & Preston, G. W. 2011, *ApJS*, 197, 29
 Frebel, A. 2010, *AN*, 331, 474
 Gonzalez, G., & Wallerstein, G. 1998, *AJ*, 116, 765
 Govea, J., Gomez, T., Preston, G. W., & Sneden, C. 2014, *ApJ*, 782, 59
 Gratton, R. G. 1982, *A&A*, 115, 171
 Gratton, R. G. 1987, *A&A*, 179, 181

- Gratton, R. G., & Ortolani, S. 1989, *A&A*, 211, 41
- Hansen, C. J., Nordström, B., Bonifacio, P., et al. 2011, *A&A*, 527, A65
- Jayasinghe, T., Kochanek, C. S., Stanek, K. Z., et al. 2018, *MNRAS*, 477, 3145
- Juresik, J., Sódor, Á, Szeidl, B., et al. 2009, *MNRAS*, 400, 1006
- Kolenberg, K., Fossati, L., Shulyak, D., et al. 2010a, *A&A*, 519, A64
- Kolenberg, K., Szabó, R., Kurtz, D. W., et al. 2010b, *ApJL*, 713, L198
- Kraft, R. P., & Ivans, I. I. 2003, *PASP*, 115, 143
- Kramida, A., Ralchenko, Yu., Reader, J. & NIST ASD Team 2018, Atomic Spectra Database, NIST Standard Reference Database 78, v.5.5.6, <https://www.nist.gov/pml/atomic-spectra-database>
- Lambert, D. L., Heath, J. E., Lemke, M., & Drake, J. 1996, *ApJS*, 103, 183
- Lawler, J. E., Guzman, A., Wood, M. P., Sneden, C., & Cowan, J. J. 2013, *ApJS*, 205, 11
- Lawler, J. E., Sneden, C., Nave, G., et al. 2017, *ApJS*, 228, 10
- Layden, A. C. 1994, *AJ*, 108, 1016
- Layden, A. C., & Sarajedini, A. 2003, *AJ*, 125, 208
- Lee, Y. S., Beers, T. C., Allende Prieto, C., et al. 2011, *AJ*, 141, 90
- Liu, S., Zhao, G., Chen, Y.-Q., Takeda, Y., & Honda, S. 2013, *RAA*, 13, 1307
- Longmore, A. J., Dixon, R., Skillen, I., Jameson, R. F., & Fernley, J. A. 1990, *MNRAS*, 247, 684
- Longmore, A. J., Fernley, J. A., & Jameson, R. F. 1986, *MNRAS*, 220, 279
- Marconi, M., Coppola, G., Bono, G., et al. 2015, *ApJ*, 808, 50
- Martínez-Vázquez, C. E., Monelli, M., Gallart, C., et al. 2016a, *MNRAS*, 461, L41
- Martínez-Vázquez, C. E., Stetson, P. B., Monelli, M., et al. 2016b, *MNRAS*, 462, 4349
- Massari, D., Mucciarelli, A., Dalessandro, E., et al. 2017, *MNRAS*, 468, 1249
- Mateo, M., Bailey, J. I., Crane, J., et al. 2012, *Proc. SPIE*, 8446, 84464Y
- Mateu, C., Vivas, A. K., Downes, J. J., et al. 2012, *MNRAS*, 427, 3374
- Monelli, M., Bernard, E. J., Gallart, C., et al. 2012, *MNRAS*, 422, 89
- Monelli, M., Fiorentino, G., Bernard, E. J., et al. 2017, *ApJ*, 842, 60
- Mucciarelli, A., Lapenna, E., Massari, D., Ferraro, F. R., & Lanzoni, B. 2015, *ApJ*, 801, 69
- Muñoz, C., Geisler, D., & Villanova, S. 2013, *MNRAS*, 433, 2006
- Musella, I., di Criscienzo, M., Marconi, M., et al. 2018, *MNRAS*, 473, 3062
- Neeley, J. R., Marengo, M., Bono, G., et al. 2017, *ApJ*, 841, 84
- O'Brian, T. R., Wickliffe, M. E., Lawler, J. E., Whaling, W., & Brault, J. W. 1991, *JOSAB*, 8, 1185
- Oosterhoff, P. T. 1939, *Obs*, 62, 104
- Pancino, E., Britavskiy, N., Romano, D., et al. 2015, *MNRAS*, 447, 2404
- Pietrukowicz, P., Kozłowski, S., Skowron, J., et al. 2015, *ApJ*, 811, 113
- Pilachowski, C. A., Sneden, C., & Wallerstein, G. 1983, *ApJS*, 52, 241
- Preston, G. W. 1959, *ApJ*, 130, 507
- Preston, G. W., & Paczynski, B. 1964, *ApJ*, 140, 181
- Preston, G. W., Sneden, C., Chadid, M., Thompson, I. B., & Shtetman, S. A. 2018, *ApJ*, submitted
- Pritzl, B. J., Armandroff, T. E., Jacoby, G. H., & da Costa, G. S. 2002, *AJ*, 124, 1464
- Pritzl, B. J., Venn, K. A., & Irwin, M. 2005, *AJ*, 130, 2140
- Reddy, B. E., Lambert, D. L., & Allende Prieto, C. 2006, *MNRAS*, 367, 1329
- Ruffoni, M. P., den Hartog, E. A., Lawler, J. E., et al. 2014, *MNRAS*, 441, 3127
- Ryabchikova, T., Piskunov, N., Kurucz, R. L., et al. 2015, *PhyS*, 90, 054005
- Sandage, A. 1958, *RA*, 5, 41
- Sesar, B. 2012, *AJ*, 144, 114
- Shappee, B. J., Prieto, J. L., Grupe, D., et al. 2014, *ApJ*, 788, 48
- Simmerer, J., Ivans, I. I., Filler, D., et al. 2013, *ApJL*, 764, L7
- Simmerer, J., Sneden, C., Cowan, J. J., et al. 2004, *ApJ*, 617, 1091
- Smith, H. A., & Manduca, A. 1983, *AJ*, 88, 982
- Sneden, C., Preston, G. W., Chadid, M., & Adamów, M. 2017, *ApJ*, 848, 68
- Sneden, C. A. 1973, PhD thesis, Univ. Texas
- Sobeck, J. S., Lawler, J. E., & Sneden, C. 2007, *ApJ*, 667, 1267
- Soszyński, I., Udalski, A., Szymański, M. K., et al. 2009, *AcA*, 59, 1
- Stetson, P. B., Braga, V. F., Dall'Ora, M., et al. 2014, *PASP*, 126, 521
- Tody, D. 1986, *Proc. SPIE*, 627, 733
- Tody, D. 1993, in *ASP Conf. Ser. 52, Astronomical Data Analysis Software and Systems II*, ed. R. J. Hanisch, R. J. V. Brissenden, & J. Barnes (San Francisco, CA: ASP), 173
- Torrealba, G., Catelan, M., Drake, A. J., et al. 2015, *MNRAS*, 446, 2251
- van Albada, T. S., & Baker, N. 1973, *ApJ*, 185, 477
- Villanova, S., Geisler, D., Carraro, G., Moni Bidin, C., & Muñoz, C. 2013, *ApJ*, 778, 186
- Walker, A. R., Andreuzzi, G., Martínez-Vázquez, C. E., et al. 2017, *AJ*, 154, 8
- Wallerstein, G., & Huang, W. 2010, *MmSAI*, 81, 952
- Wood, M. P., Lawler, J. E., Sneden, C., & Cowan, J. J. 2013, *ApJS*, 208, 27
- Wood, M. P., Lawler, J. E., Sneden, C., & Cowan, J. J. 2014, *ApJS*, 211, 20
- Zinn, R. 1980, *ApJS*, 42, 19
- Zinn, R., & West, M. J. 1984, *ApJS*, 55, 45